RESEARCH   **Open Access**

Optical satellite sensor and positioning accuracy analysis for the Hongqi-1-H9 wide-range satellite in different terrains

Wenping Song[1], Jianxiong Wang[2*], Yang Bai[3], Linhui Wang[4], Xiang Li[3], Shiqiang Tian[3] and Xianyang Qi[3]

*Correspondence:
jianxiongw@126.com
[2] Water Conservancy
Academy, Yunnan
Agricultural University,
452 Fengyuan Road,
Kunming 650201, China
Full list of author information
is available at the end of the
article

Abstract

The excellent performance of geometric positioning of a newly launched satellite will greatly broaden its application field. Launched on January 15, 2020, the Hongqi-1-H9 wide-range satellite is the largest sub-meter-level satellite worldwide and the first ton-level commercial remote sensing satellite in China, with a resolution of less than 1 m and a swath width of 136 km. This study was aimed at assessing the geometric positioning accuracy of this newly launched satellite considering three aspects, namely, the circle error accuracy, rational polynomial coefficient-based direct geometric positioning accuracy and ground control point-based absolute positioning accuracy under urban, plain, and mountainous areas, with different topographies. The results of the conducted experimental investigation indicated that the Hongqi-1-H9 satellite could exhibit a high positioning accuracy in planar and vertical directions for different terrains. In particular, for our experimental areas with a low topography and few surface structures, the geometric positioning accuracy of the Hongqi-1-H9 satellite imagery was less than 4m and 2 m in the planimetry and elevation directions, respectively. These characteristics can promote the application of the Hongqi-1-H9 satellite images in agricultural surveys, target detection, and land surveys, among other domains.

Keywords: Geometric positioning, Different terrains, The Hongqi-1-H9 satellite, Accuracy analysis

1 Introduction

Despite the rapid advancement in satellite remote sensing technology, two key requirements to obtain high-spatial-resolution satellite images remain to be attained [1–3]. The first requirement corresponds to the fixed-point fast revisit capability, which is primarily influenced by the timeliness of the satellites [4, 5]; for instance, satellites can generally provide real-time images of disaster areas within a few minutes in natural disaster events [6]. The second requirement corresponds to the prompt updating capacity for a large-scale area, which mainly depends on the swath width of the satellite. This aspect can facilitate the rapid monitoring of construction areas [7, 8], daily distribution survey of marine vessels [9], and agricultural surveys, among other applications, in which large-scale time series satellite images must be acquired in a small period.

Changguang is in the process of deploying the "Jilin-1" optical remote sensing satellite constellation in two phases [10, 11]: The first phase involves placing 60 satellites in orbit, thereby allowing the revisitation of key regions worldwide within 30 min and the observation of more than 800 target areas worldwide every day. In the second phase, 138 satellites will be present in orbit, thereby enabling the revisitation of any area worldwide within 10 min. The first batch of satellites of the "Jilin-1" optical remote sensing constellation, including the optical A satellite, smart video 01/02 satellite, and smart verification satellite, was launched successfully on October 15, 2015, and these satellites have been in orbit for 4.5 years. Subsequently, the video 03–08 satellites were launched sequentially. The Jilin-1KF01A satellite (the Hongqi-1-H9 wide-range satellite, hereafter referred to as the Hongqi-1-H9 wide-range satellite), which was successfully launched on January 15, 2020, is the largest sub-meter-level satellite worldwide and the first ton-level commercial remote sensing satellite in China, with a resolution of less than 1 m and a swath width of 136 km. The Hongqi-1-H9 wide-range satellite can acquire sub-meter image data at a rate of approximately 1000 km^2 per second and the full-coverage image information for an area of more than 1000,000 km^2. The sensor information for the Hongqi-1-H9 wide-range satellite is presented in Table 1 [12].

In general, the resolution and swath width of satellite images are inversely related, that is, the swath width decreases as the resolution increases [13]. Conventionally, the satellite swath width is increased by stitching multiple lenses whose optical axis does not point to the center of the Earth [10]. However, this type of optical imaging system is only suitable when the field of view is not excessively large (approximately 10°). According to Table 1, the field of view of the Hongqi-1-H9 wide-range satellite is 16.1°. Consequently, applying multi-lens stitching may significantly increase the difference in the pixel resolution between the edge and center of the image plane [14]. Moreover, the shift differences in the images caused by the curvature and rotation of the Earth, among other factors, may lead to different sampling effects at different viewing positions, leading to a deteriorated image quality [15]. The Hongqi-1-H9 wide-range satellite avoids the projection distortion caused by multiple lenses by using a single lens whose optical axis points to the center of the Earth. In this case, the resolutions of the center and edge of the field of view are nearly equivalent, thereby facilitating the image processing [13].

Nevertheless, a single lens cannot be used to achieve a focal length of 4850 mm and field of view of 16.1°. In particular,the Hongqi-1-H9 wide-range adopts the Cook three-mirror anastigmat (TMA) system. As shown in Fig. 1 [16–18], the Cook TMA imaging system is mainly composed of three mirrors: primary mirror, secondary mirror and

Table 1 Characteristics of the Hongqi-1-H9 wide-range satellite

Specification	Panchromatic	Multispectral
Field of view	16.1°	16.1°
Focal length	4850 mm	4850 mm
Ground sample distance	0.75 m	3.0 m
Swath width	136 km	136 km
Attitude stability	< 0.0005°/s	< 0.0005°/s
Signal–noise ratio	>100:1	>100:1

Song *et al. J Wireless Com Network*   (2021) 2021:3

Page 3 of 15

Fig. 1 Cook TMA system
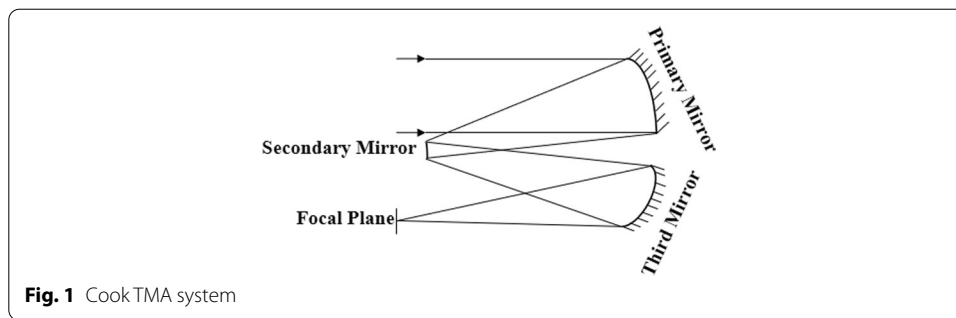
third mirror. The main purpose is to minimize the impact of three optical aberrations including spherical aberration, coma aberration, and astigmatism on sensor imaging. Furthermore, the Cook TMA system can eliminate the central block from the aperture by increasing the off-axis field of view [17]. Such that, the clear aperture of the field of view and the mirror is completely off-axis, forming a coaxial system in which the field of view and aperture are off-axis. So the integration of three mirrors not only can reduce the aberrations, but also greatly enhance the field of view. In this configuration, the position change between any two mirrors approximately 1 m apart is not more than 5 μm, the shape of the large aspheric mirror corresponds to a wavelength of more than 1/50, and the original dynamic modulation transfer function is larger than 0.16 [12]. Consequently, the imaging clarity and geometric accuracy can be enhanced even when vibration and temperature changes occur.

The geometric positioning accuracy is very important for a newly launched satellite sensor, and the excellent performance of geometric positioning of a newly launched satellite will greatly broaden its application field. Considering the characteristics of the Hongqi-1-H9 wide-range satellite, the objective of this study was to evaluate a novel optical satellite sensor and analyze the geometric positioning accuracy of the Hongqi-1-H9 wide-range satellite in areas with three different topographies, specifically, urban, plain, and mountainous areas. From the experimental study, several conclusions were obtained regarding the newly launched Hongqi-1-H9 wide-range satellite. It was noted that the basic product could realize regional mapping and meet the application requirements. The contributions of this paper are as follow: (1) The imagery obtained through the newly launched Hongqi-1-H9 wide-range satellite was evaluated and analyzed in terms of the circle error (CE) accuracy, vendor-provided rational polynomial coefficient (RPC)-based direct geometric positioning accuracy and ground control point (GCP)-based absolute positioning accuracy; (2) The experimental results are comprehensively compared in three different terrains.

The remaining paper is organized as follows. After the introduction of the Hongqi-1-H9 wide-range satellite, Sect. 2 introduces the geometric positioning methods and criteria. Section 3 describes the study area and data used. The experimental results and discussions are presented in Sect. 4, and the concluding remarks are presented in Sect. 5.

2 Methods

Generally, satellite images can be used to analyze the geometric positioning accuracy by using two approaches [20]. In the first approach, high-performance sensor structures and parameters can be used to realize the geometric transformation from the

image space to the ground space [21–23]. The second approach is based on the use of a rational function model (RFM), which exploits the constraints between different images [25–27]. Nevertheless, the error contained in the RPCs may destroy the photogrammetric relation and deteriorate the geometric performance of the obtained high-resolution images. In particular, the accuracy of the first evaluation approach is more accurate. In this work, a data-driven evaluation method was employed, as described in the following subsections.

2.1 Preprocessing

In general, the vendor-provided RPCs can replace the position and attitude parameters of satellite sensors [28]. Different RPCs for different data processing phases, containing different degrees of errors, can be defined according to the exterior orientation parameters by using the rigorous sensor model (RSM) [29, 30]. In this study, the existing RPCs were extracted through radiation and geometric correction. These RPCs were solved using a terrain-independent method. Specifically, first, image grids were established in the image space, and later, a three-dimensional (3D) coordinate grid area was established in the ground space. In this process, the RSM calculated the point coordinates of the ground grids, and the ground 3D grids were divided into more than three layers in the elevation direction. Finally, the RPCs were calculated using the least squares method according to the established image and ground grids [31]. For convenience, all the satellite imagery data, GPS points, and accuracy results were defined according to the World Geodetic System 1984.

2.2 RPCs-based block adjustment model

The RFM is a traditional expression of the satellite sensor model, in which rational polynomials are used to ensure the correspondence between the image and ground points, as indicated in Eq. (1).

$$
\begin{cases}
x_n = \dfrac{Num_1(B_n, L_n, H_n)}{Den_1(B_n, L_n, H_n)} \\[2ex]
y_n = \dfrac{Num_2(B_n, L_n, H_n)}{Den_2(B_n, L_n, H_n)}
\end{cases}
\tag{1}
$$

where (x_n, y_n) represent normalized image coordinates, corresponding to the normalized coordinates (B_n, L_n, Z_n) in the ground space. $Num_i(B_n, L_n, Z_n)(i = 1, 2)$ and $Den_i(B_n, L_n, Z_n)(i = 1, 2)$ denote the rational polynomials. As described in literature [32], linear polynomials are used to correct the distortions caused be optical projection; quadratic polynomials are used to correct the errors induced by the Earth curvature, lens distortion, and atmospheric refraction; and the other unknown distortions are compensated using the cubic polynomial.

Compared with that in ground space, the compensation in image space is more rigorous theoretically [33], as indicated in Eq. (2).

Song *et al. J Wireless Com Network*   (2021) 2021:3

Page 5 of 15

$$\begin{cases} x' = a_0 + a_1x + a_2y \\ y' = b_0 + b_1x + b_2y \end{cases} \tag{2}$$

where (x', y') denote the image points measured corresponding to the ground points; (x, y) denote the image coordinate values of the ground points calculated using Eq. (2); (a_0) and (b_0) denote the shift orientation parameters; and $a_i(i = 0, 1, 2)$ and $b_i(i = 0, 1, 2)$ denote the affine transformation orientation parameters, where $a_i(i = 0, 1, 2)$ and $b_i(i = 0, 1, 2)$ are used to correct errors in column and row directions, respectively.

Therefore, the RPCs-based block adjustment model can be constructed in matrix form as shown in Eq. (3), according to Eqs. (1) and (2) [34, 35]:

$$V = At + BX - L \tag{3}$$

where

$$V = \begin{bmatrix} V_x & V_y \end{bmatrix}^T$$

$$A = \begin{bmatrix} \dfrac{\partial x}{\partial a_0} & \cdots & \dfrac{\partial x}{\partial a_1} & \dfrac{\partial x}{\partial a_2} \\ \dfrac{\partial y}{\partial b_0} & \cdots & \dfrac{\partial y}{\partial b_1} & \dfrac{\partial y}{\partial b_2} \end{bmatrix}$$

$$B = \begin{bmatrix} \dfrac{\partial x}{\partial B_n} & \dfrac{\partial x}{\partial L_n} & \dfrac{\partial x}{\partial Z_n} \\ \dfrac{\partial y}{\partial B_n} & \dfrac{\partial y}{\partial L_n} & \dfrac{\partial y}{\partial Z_n} \end{bmatrix}$$

$$t = \begin{bmatrix} \Delta a_0 & \Delta a_1 & \Delta a_2 & \Delta b_0 & \Delta b_1 & \Delta b_2 \end{bmatrix}^T$$

$$X = \begin{bmatrix} \Delta B_n & \Delta L_n & \Delta H_n \end{bmatrix}^T$$

2.3 Accuracy evaluation

In this work, the geometric positioning accuracy of the Hongqi-1-H9 wide-range satellite imagery under three different terrains was evaluated considering control-based and non-control-based geometric positioning accuracies. Among these, the non-control-based geometric positioning accuracy included two parts: accuracy evaluation based on circular probability errors and on direct forward intersection by using vendor-provided RPCs [36, 37].

To examine the control-based geometric positioning accuracy and that based on direct forward intersection by using the vendor-provided RPCs, high-precision Global Positioning System (GPS) measured points $(B_{GPS}, L_{GPS}, H_{GPS})$ and their corresponding solved coordinate values $(B_i, L_i, H_i)(i = 1, 2, \cdots, n)$ were determined to obtain the root mean squared errors (RMSEs), as shown in Eq. (4).

$$\begin{cases} RMSE_B = \sqrt{\dfrac{\sum_{i=1}^{n}(B_{GPS} - B_i)^2}{n}} \\[3mm] RMSE_L = \sqrt{\dfrac{\sum_{i=1}^{n}(L_{GPS} - L_i)^2}{n}} \\[3mm] RMSE_H = \sqrt{\dfrac{\sum_{i=1}^{n}(H_{GPS} - H_i)^2}{n}} \end{cases} \tag{4}$$

The accuracy evaluation based on circular probability errors [38] was performed in three phases. (1) Obtaining two geometric positioning error sets X and Y in the longitude and latitude directions, respectively, which correspond to the differences between the point coordinates measured on the image and the corresponding GPS measured points. (2) Determining the means μ_x and μ_y, RMSEs σ_x and σ_y, and correlation coefficient ρ for sets X and Y. (3) Ensuring that the geometric positioning errors with systematic errors and strong correlations in all the directions follow a normal distribution. The joint density function in the polar coordinate system was defined as in Formula (5) [39]:

$$\frac{1}{2\pi\sigma_x\sigma_y\sqrt{1-\rho^2}} \int_0^{CE90} \int_0^{2\pi} r * exp\left\{ -\frac{1}{2(1-\rho)} \left[\frac{(rcos\theta - \mu_x)^2}{\sigma_x^2} \right. \right.$$

$$\left. \left. -\frac{2\rho(rcos\theta - \mu_x)(rsin\theta - \mu_y)}{\sigma_x\sigma_y} + \frac{(rsin\theta - \mu_y)^2}{\sigma_y^2} \right] \right\} drd\theta = P \tag{5}$$

where

$$X = rcos\theta$$
$$Y = rsin\theta$$
$$r = \sqrt{(X^2 + Y^2)}$$

The CE90 was solved to measure the non-control-based geometric positioning accuracy.

3 Study area and data

The considered study areas are located in three regions with different terrains in China (Fig. 2). The urban area has many high-rise buildings, and the plain and mountainous areas have rough terrains. These feature ranges are considerably different in terms of the terrains and surface coverage. The urban, plain, and mountainous study areas cover approximately 550 km^2, 600 km^2, and 720 km^2, respectively. The urban and plain areas traverse the altitudinal range of 0–150 m. The mountainous area exhibit a high variability of slopes with varying orientations of the ridges and deep valleys; moreover, this area includes few notable water bodies.

The satellite images of the three study areas were acquired during the winter when the surface vegetation coverage was relatively simple. Moreover, the overlaps of the stereo images for the three areas were more than 80%, and the ground sampling distance was approximately 0.75 m. Figure 2 illustrates the coverage of the three study areas with different terrains in China. The urban area ranged from 121.267°E to 121.592°E and from 30.018°N to 31.316°N in the longitudinal and latitudinal directions, respectively, and the
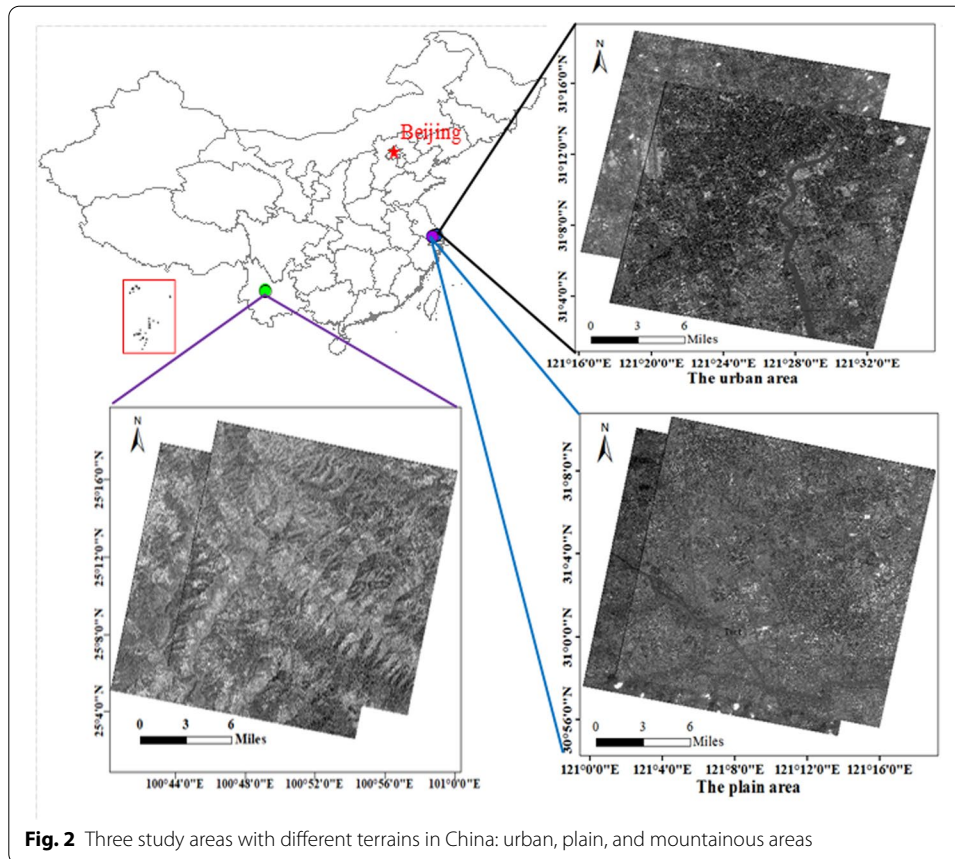
Fig. 2 Three study areas with different terrains in China: urban, plain, and mountainous areas

imagery data were collected in February 2020. The plain area ranged from 120.90°E to 121.338°E and from 30.90°N to 31.20°N in the longitudinal and latitudinal directions, respectively, and the satellite imagery data were collected in 2020, with a field of view of 16.1°. The mountainous area ranged from 100.60°E to 101.228°E and from 25.042°N to 25.3°N in the longitudinal and latitudinal directions, respectively, and the satellite imagery data were acquired in March, 2020.

To perform absolute accuracy assessments, accurate and independent reference data are required [40, 41]. The reference data should be at least three times more accurate than the evaluated data [42]. Therefore, in this work, we considered high-quality GPS points, which satisfy the accuracy requirement, and thus, do not adversely affect the evaluation. For the urban, plain, and mountainous areas, the number of GPS points for the comparative experiments and accuracy assessment was 32, 18, and 25, respectively.

4 Results and discussion

To analyze the geometric positioning accuracy of the Hongqi-1-H9 satellite imagery in three different terrains, the control-based accuracy and the non-control-based accuracy are regarded as two significant evaluation criteria. For the control-based accuracy, it has been used many engineering application fields, such as mapping and navigation. And the non-control-based accuracy indicates the performance of geometric location without introducing any aided information such as GPS measured points into the bundle

adjustment process. Excellent non-control positioning performance be greatly time-saving and cheap in the engineering application areas where effective control information cannot be obtained. In this study, the non-control-based geometric positioning accuracy was evaluated based on circular probability errors and residuals of direct forward intersection.

4.1 Analysis of geometric positioning accuracy without ground control points

The geometric positioning accuracy of the Hongqi-1-H9 wide-range satellite imagery without using ground control points involved two parts: accuracy evaluation based on circular probability errors and that of the direct forward intersection by using vendor-provided RPCs.
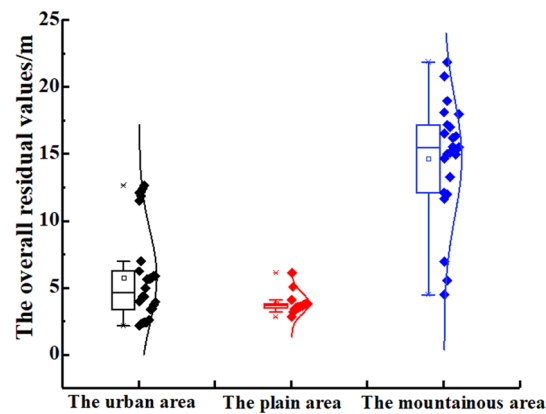
4.1.1 Accuracy analysis based on circular probability errors

The accuracy based on the circular probability errors was calculated according to the three phases described in Sect. 2.3. The residuals, including the errors in the latitude and longitude directions, for the Hongqi-1-H9 wide-range satellite imagery under three different terrains are illustrated in Fig. 3. In Fig. 3, the x and y axes denote the residual values for the three study areas and the corresponding residual counts, respectively. In addition, the residual fitting results for the Hongqi-1-H9 wide-range satellite imagery under three different terrains, obtained using normal distribution functions, are presented. It can be noted that the circular probability error-based accuracy for the plain area has smaller confidence intervals in all the directions compared to those for the urban and mountainous areas. In particular, in the latitudinal direction, except for certain outliers caused by human factors, the geometric positioning accuracies of the Hongqi-1-H9 wide-range satellite imagery in the plain and urban areas are approximately 3–5 m and less than 7 m, respectively, which are considerably superior than the accuracy for the mountainous area (approximately 10–16 m), nearly consistent with the positioning accuracy in the longitudinal direction. Moreover, in the longitudinal direction, the Hongqi-1-H9 wide-range satellite images in the plain and urban areas exhibit nearly equivalent positioning performances (less than 5 m). The planar geometric positioning accuracy for the plain area is slightly superior than that for the urban area, although it is considerably higher than that for the mountainous area, as shown in Fig. 4. A possible explanation for this difference is that the stereo images in the mountain area have a weak intersection angle, which decreases the geometric positioning performance to a certain extent. In other words, the positioning performance in the mountainous area can be improved by improving the intersection condition.

   Table 2 summarizes the results of the geometric positioning based on the circular probability errors. It can be noted that the images pertaining to the plain area (CE90 4.5051 m) correspond to a slightly higher positioning performance than that for the urban area (CE90 6.7216 m) and exhibit a smaller span of residuals, indicating the higher stability of positioning in the plain area. However, for the mountainous area, the maximum circular probability error in the planimetry direction is 15.5212 m. Therefore, the Hongqi-1-H9 wide-range satellite imagery can exhibit a circle probability error-based accuracy of less than 5 m, less than 7 m, and 15.5212 m in the plain, urban, and mountainous areas, respectively.
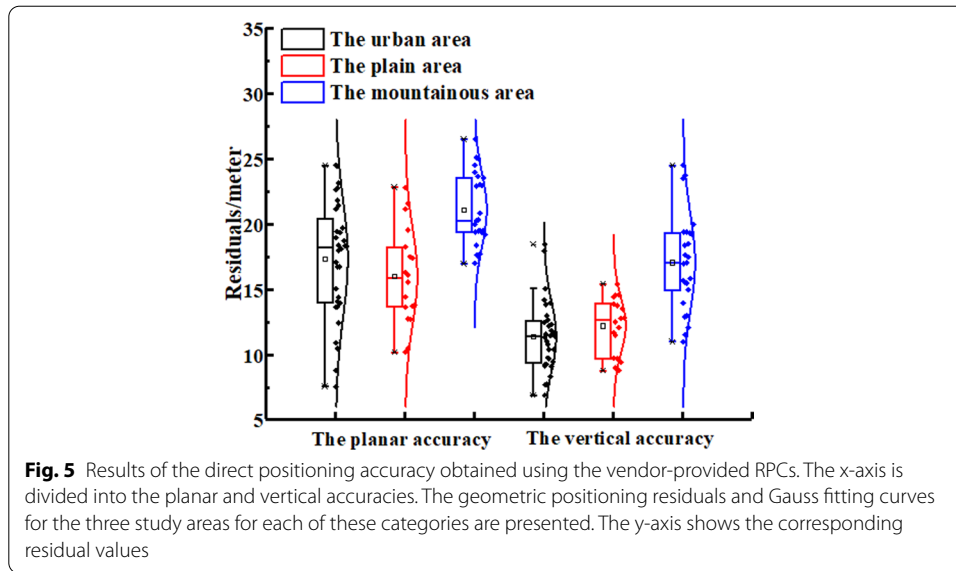
Song *et al. J Wireless Com Network*   (2021) 2021:3

Page 9 of 15
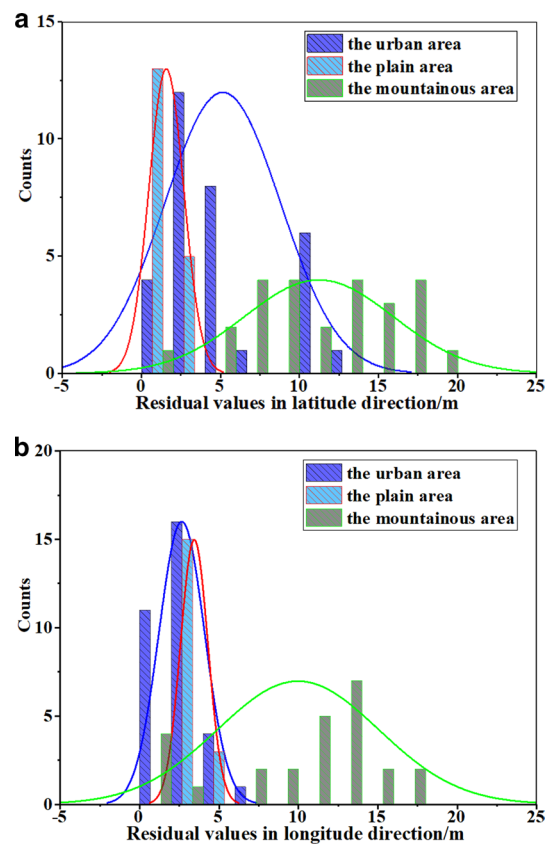
Fig. 3 Residuals of the Hongqi-1-H9 imagery under three different terrains in latitude and longitude.x and y axes correspond to the residual values of three different areas and the corresponding residual counts, respectively

Fig. 4 Overall residual values of the Hongqi-1-H9 wide-range satellite imagery under three different terrains

Table 2 Accuracy evaluation based on circular probability errors

Area	Urban	Plain	Mountainous
CE90/m	6.7216	4.5051	15.5212

Fig. 5 Results of the direct positioning accuracy obtained using the vendor-provided RPCs. The x-axis is divided into the planar and vertical accuracies. The geometric positioning residuals and Gauss fitting curves for the three study areas for each of these categories are presented. The y-axis shows the corresponding residual values

Table 3 Mean errors and RMSEs of the direct forward intersection, obtained using the vendor-provided RPCs, for three different terrains

Category	Urban area		Plain area		Mountainous area	
Direction	Planar/m	Vertical/m	Planar/m	Vertical/m	Planar/m	Vertical/m
Mean error	17.3303	11.3748	15.9954	12.2240	21.0881	17.0761
RMSEs	17.8739	11.6761	16.3902	12.3994	21.2616	17.4499

4.1.2 Accuracy analysis of direct forward intersection by using vendor-provided RPCs

After the radiometric correction, the vendor-provided RPCs were extracted from the structures and parameters of the RSM, which can be used to construct the RFM for the geometric positioning by replacing the RSM. In the experimental evaluation of the direct forward intersection using the vendor-provided RPCs, the accuracy of all the GPS points was less than 5 cm, and the weights were considered to be equivalent. For the corresponding feature points, high-criteria manual selection was adopted to ensure the sub-pixel-level characteristics, which can satisfy the requirements of the geometric positioning.

Figure 5 shows the results for the direct positioning accuracy obtained using the vendor-provided RPCs in the World Geodetic System 1984. The x-axis is separated into the planar and vertical accuracies, for each of which, the geometric positioning residuals and Gauss fitting curves of the three study areas are shown in the figure. The y-axis shows the corresponding residual values. It can be noted that the error values in both the planimetry and elevation directions are similar, even though the positioning accuracy in the mountainous area is worse than that in the plain and urban areas. Specifically, as indicated in Table 3, for the urban area, the mean errors in the planimetry and elevation directions are 17.3303 m and 11.3748 m, and the RMSEs are 17.8739 m and 11.6761 m, respectively. Similar to these values, the plain area exhibits, in the planimetry and vertical directions, mean errors of 15.9954 m and 12.2240 m, and RMSEs of 16.3902

Table 4 Results of the absolute positioning accuracy for the Hongqi-1-H9 wide-range satellite under different terrains

RMSEs	Directions		
	Latitude	Longitude	Elevation
Urban area/ m	3.4815	4.4756	2.7262
Plain area/m	3.2448	1.6639	1.7466
Mountainous area/m	4.2622	4.9386	4.9217

m and 12.3994 m, respectively. In the mountainous area, the planar and vertical RMSEs are 21.2616 m and 17.4499 m, respectively. Overall, for all three terrains, the geometric positioning accuracy determined using the vendor-provided RPCs is less than 20 m and 15 m in the planimetry and vertical directions, respectively.

Moreover, the accuracy of the direct forward intersection obtained using the vendor-provided RPCs was worse than that based on the circular probability errors, as indicated by the comparison of the values presented in Tables 2 and 3. A possible explanation for this difference is that the vendor-provided RPCs still contain systematic errors, which considerably deteriorate the geometric positioning. Furthermore, the angles for the cross track stereo images are influence the direct positioning accuracy. In this regard, the geometric positioning accuracy can be improved by reducing the system errors in the vendor-provided RPCs.

4.2 Analysis of the absolute positioning accuracy

The absolute geometric positioning accuracy can be evaluated considering external orientation elements or GCPs, using the external reference values as a comparison benchmark to reflect the deviation indicated by the RMSEs. As a significant evaluation criterion, it can indicate the accuracy and performance of the satellite imagery for any geometric location. As mentioned previously, 32, 18, and 25 GPS points were measured for the urban, plain, and mountainous areas, respectively. In this experiment, five GPS points having nearly equivalent distributions were selected as the control points, and the remaining GPS points were used to evaluate the accuracy. Moreover, the affine transformation model was used for the bias compensation in the image space.

Figure 6 shows the geometric positioning error bar graphs using the five GCPs. The black crosses represent the point positions in the World Geodetic System 1984, and the blue and red arrows indicate the plane and elevation errors, respectively. As shown in Fig. 5, the Hongqi-1-H9 wide-range satellite imagery under three different terrains exhibit different geometric positioning performances, all of which are sufficient to realize high-resolution mapping.

The results of the absolute positioning accuracy are summarized in Table 4. The geometric positioning accuracy is presented in terms of the latitudinal, longitudinal, and vertical direction. From Table 4, it can be noted that the Hongqi-1-H9 wide-range satellite exhibits the highest geometric positioning performance in the plain area, with a positioning accuracy of 3.2448 m, 1.6639 m, and 1.7466 m in the latitudinal, longitudinal, and elevation directions, respectively, when using the five GPS points. For the urban area, the positioning accuracy is slightly poor: 3.4815 m, 4.4756 m, and 2.7262 m in the
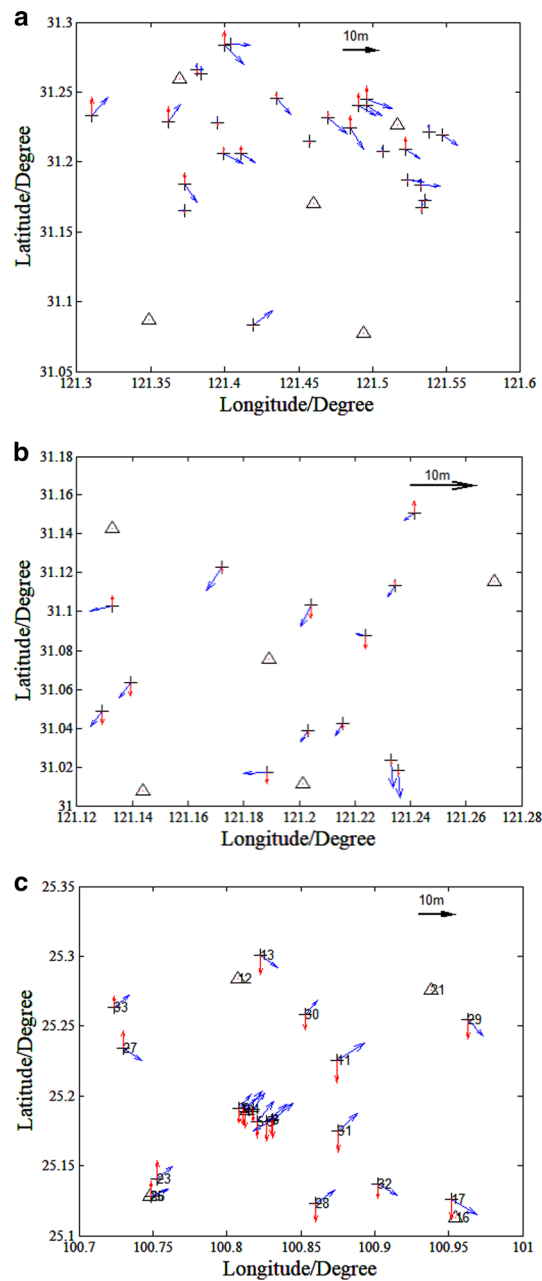
Fig. 6 Geometric positioning error bar graphs when using five GCPs. The black crosses represent the point positions in the World Geodetic System 1984, and the blue and red arrows indicate the plane and elevation errors, respectively. **a–c** show the results for the urban, plain, and mountainous areas, respectively

latitudinal, longitudinal, and elevation directions, respectively. The worst geometric positioning corresponds to the mountainous area, with accuracies of 4.2622 m, 4.9386 m, and 4.9217 m in the latitudinal, longitudinal, and elevation directions, respectively. Overall, based on the experimental data, it can be considered that the Hongqi-1-H9 wide-range satellite imagery can achieve a high positioning accuracy in the planar and vertical directions under different terrains. Specifically, for areas with a low topography

and few surface structures, the geometric positioning accuracy of the Hongqi-1-H9 wide-range satellite imagery can be less than 4 m and 2 m in the planimetry and elevation directions, and thus, the Hongqi-1-H9 wide-range satellite images exhibit the excellent performance of geometric positioning and can be applied to many science experiments and engineering applications in the future, such as land surveying and mapping, agricultural estimation and analysis, target detection, and such applications.

5 Conclusions

In this work, we attempt to exam the positioning accuracy for the Hongqi-1-H9 wide-range satellite images under regions with three different topographies, specifically, urban, plain, and mountainous areas. Three different main experiments were performed. The experimental results clarified the geometric positioning performance under three different areas with different terrains. From these findings, several key conclusions were drawn as follows:

(1) In the experiments, the Hongqi-1-H9 satellite imagery could achieve a circle probability error-based accuracy of less than 16 m without using any GCPs, which is sufficient for medium resolution mapping.

(2) Under all three terrains, the residuals of forward intersection based on RFM was less than 20 m and approximately 15 m in planar and vertical directions, respectively, and the positioning accuracy in mountainous area was still worse than in plain and urban areas.

(3) The Hongqi-1-H9 satellite imagery could achieve a high absolute positioning accuracy in planar and vertical directions under different terrains. In particular, for our experimental areas with a low topography and few surface structures, the absolute positioning accuracy was less than 4 and 2 m in planar and vertical directions, respectively.

Overall, the Hongqi-1-H9 satellite exhibits not only an excellent fixed-point revisitation capability and prompt updating capacities for a large-scale area, but also a high positioning performance through the across-track stereo imagery. In future research, the Hongqi-1-H9 satellite can be used in many science experiments and engineering applications, such as land surveying and mapping, agricultural estimation and analysis, target detection, and such applications.

Author details

[1] College of Surveying and Geo-informatics, Tongji University, 1239 Siping Road, Shanghai 200092, China. [2] Water Conservancy Academy, Yunnan Agricultural University, 452 Fengyuan Road, Kunming 650201, China. [3] Changguang Satellite Technology Co., LTD, 1299 Mingxi Road, Changchun 130102, China. [4] School of Electronics and Information Engineering, Hunan University of Science and Engineering, 130 Yangzitang Road, Yongzhou 425199, China.

References

1. J.C. White, N.C. Coops, M.A. Wulder, M. Vastaranta, T. Hilker, P. Tompalski, Remote sensing technologies for enhancing forest inventories: a review. Can. J. Remote Sens. **42**(5), 619–641 (2016)
2. T.E. Shaw, S. Gascoin, P.A. Mendoza, F. Pellicciotti, J. McPhee, Snow depth patterns in a high mountain Andean catchment from satellite optical tristereoscopic remote sensing. Water Resour. Res. **56**(2), 1–23 (2020)
3. J. Wang, D. Yang, M. Detto, B.W. Nelson, M. Chen, K. Guan, J. Wu, Multi-scale integration of satellite remote sensing improves characterization of dry-season green-up in an Amazon tropical evergreen forest. Remote Sens. Environ. **246**, 865–881 (2020)
4. W.G. Han, J. Matthew, Near real-time satellite data quality monitoring and control, in *2016 IEEE International Geoscience and Remote Sensing Symposium (IGARSS)* (2016), pp. 206–209
5. T.M. Pham, R. Farrell, L. Tran, Revisiting the MIMO capacity with per-antenna power constraint: fixed-point iteration and alternating optimization. IEEE Trans. Wirel. Commun. **18**(1), 388–401 (2018)
6. N. Said, K. Ahmad, M. Riegler, K. Pogorelov, L. Hassan, N. Ahmad, N. Conci, Natural disasters detection in social media and satellite imagery: a survey. Multimed. Tools Appl. **78**(22), 31267–31302 (2019)
7. K. Ravindra, S. Mor, Rapid monitoring and evaluation of a community-led total sanitation program using smartphones. Environ. Sci. Pollut. Res. **25**(32), 31929–31934 (2018)
8. B. Jiang, J.C. Yang, Z.H. Lv, H.B. Song, Wearable vision assistance system based on binocular sensors for visually impaired users. IEEE Internet Things J. **6**(2), 1375–1383 (2019)
9. A.J. Zellmer, H. Burdick, I. Medel, I.I. Pondella, T. Ford, Aerial surveys and distribution models enable monitoring of fishing in marine protected areas. Ocean Coast. Manag. **165**, 298–306 (2018)
10. Super strong earth scanner-"Hongqi-1-H9" wide satellite began on-orbit debugging. https://xw.qq.com/cmsid/20200116A0V8GI00. Accessed on 27 May 2020
11. L.L. Wang, B. Yang, P. Zheng, W.S. Guan, H.Y. Wang, On-orbit relative radiometric calibration method of video satellite. Infrared Laser Eng. **47**(8), 7003–7009 (2018)
12. Chang Guang Satellite Technology Co., LTD. http://www.charmingglobe.com/. Accessed on 29 May 2020
13. J.H. Lim, J.W. Lee, T.K. Ryu, H.C. Lee, S.G. Lee, Optimal design of the reflector antenna to improve performance of C-band quad-Pol ScanSAR systems. J. Electromagn. Eng. Sci. **20**(2), 155–157 (2020)
14. J.P. Jhan, J.Y. Rau, N. Haala, M. Cramer, Investigation of parallax issues for multi-lens multispectral camera band co-registration. Int. Arch. Photogramm. Remote Sens. Spatial Inf. Sci. **42**, 157–163 (2017)
15. G. Zhang, K. Xu, P. Jia, X. Hao, D.R. Li, Integrating stereo images and laser altimeter data of the ZY3-02 satellite for improved earth topographic modeling. Remote Sens. **11**(20), 2453–2470 (2019)
16. Q.Y. Meng, H.Y. Wang, Z.Q. Yan, Residual aberration correction method of the three-mirror anastigmat (TMA) system with a real exit pupil using freeform surface. Opt. Laser Technol. **106**, 100–106 (2018)
17. L.G. Cook, Wide field of view three-mirror anastigmat (TMA) employing spherical secondary and tertiary mirrors, in *Recent Trends in Optical Systems Design and Computer Lens Design Workshop*. International Society for Optics and Photonics (1987), pp. 158–162
18. B. Jiang, J.C. Yang, H.F. Xu, H.B. Song, G. Zheng, Multimedia data throughput maximization in Internet-of-Things system based on optimization of cache-enabled UAV. IEEE Internet Things J. **6**(2), 3525–3532 (2019)
19. V.I. Zavarzin, Y.S. Mitrofanova, System solutions for prospective hyperspectral equipment. J. Opt. Technol. **84**(4), 226–230 (2017)
20. M. Wang, Y. Zhu, S. Jin, J. Pan, Q. Zhu, Correction of ZY-3 image distortion caused by satellite jitter via virtual steady reimaging using attitude data. ISPRS J. Photogramm. Remote Sens. **119**, 108–123 (2016)
21. H.B. Pan, C. Tao, Z.R. Zou, Precise georeferencing using the rigorous sensor model and rational function model for ZiYuan-3 strip scenes with minimum control. ISPRS J. Photogramm. Remote Sens. **119**, 259–266 (2016)
22. W.C. Huang, G. Zhang, D.R. Li, Robust approach for recovery of rigorous sensor model using rational function model. IEEE Trans. Geosci. Remote Sens. **54**(7), 4355–4361 (2016)
23. R.L. Kirk, J.M. Barrett, D.E. Wahl, I. Erteza, C.V. Jackowatz, D.A. Yocky, G.W. Paterson, A semi-rigorous sensor model for precision geometric processing of mini-RF bistatic radar images of the moon. Int. Arch. Photogramm. Remote Sens. Spatial Inf. Sci. **41**, 425–441 (2016)
24. K. Al-Durgham, D.D. Lichti, G. Kuntze, J. Ronsky, Rigorous accuracy assessment for 3D reconstruction using time-series dual fluoroscopy (DF) image pairs. Videometrics, range imaging, and applications XIV. Int. Soc. Opt. Photon. **10332**, 203–209 (2017)
25. S. Liu, X.H. Tong, F. Wang, W. Sun, C. Guo, Z. Ye, P. Chen, Attitude Jitter Detection Based on Remotely Sensed Images and Dense Ground Controls: A Case Study for Chinese ZY-3 Satellite. IEEE J. Sel. Top. Appl. Earth Obs. Remote Sens. **9**(12), 5760–5766 (2016)
26. H.B. Pan, S.Y. Zou, L.Y. Guan, Block adjustment with drift compensation for rational function model. Photogramm. Eng. Remote Sens. **84**(12), 791–799 (2018)

27. X. Ling, Y. Zhang, J. Xiong, X. Huang, Z. Chen, An image matching algorithm integrating global SRTM and image segmentation for multi-source satellite imagery. Remote Sens. **8**(8), 747–763 (2016)
28. S. Hou, Y. Huang, G. Zhang, R. Zhao, P. Jia, Feasibility of replacing the range doppler equation of spaceborne synthetic aperture radar considering atmospheric propagation delay with a rational polynomial coefficient model. Sensors **20**(2), 553–569 (2020)
29. K. Di, B. Liu, M. Jia, Z. Liu, Geopositioning precision analysis of multiple image triangulation using LRO NAClunar images. Int. Arch. Photogramm. Remote Sens. Spatial Inf. Sci. **41**, 369–387 (2016)
30. H.B. Pan, S.Y. Zou, L.Y. Guan, Block adjustment with drift compensation for rational function model. Photogramm. Eng. Remote Sens. **84**(12), 791–799 (2018)
31. Z.H. Zhong, S. Xu, Y. Zhang, Y. Han, L. Xu, Rational polynomial coefficients generation for high resolution Ziyuan-3 imagery, in *2017 IEEE 14th international conference on networking, sensing and control (ICNSC)* (2017), pp. 691–695
32. X.H. Tong, S.J. Liu, H. Xie, H. Wang, P. Chen, F. Bao, Geometric integration of aerial and QuickBird imagery for high accuracy geopositioning and mapping application: a case study in Shanghai. Mar. Geod. **33**(4), 437–449 (2010)
33. C.B. Liu, D. Li, N. Xue, Surveying satellite imagery RPC block adjustment without ground control points. Hydrogr. Surv. Chart. **38**(6), 17–20 (2018)
34. C. Li, X. Liu, Y. Zhang, Z. Zhang, A stepwise-then-orthogonal regression (STOR) with quality control for optimizing the RFM of high-resolution satellite imagery. Photogramm. Eng. Remote Sens. **83**(9), 611–620 (2017)
35. S.J. Tang, B. Wu, Q. Zhu, Combined adjustment of multi-resolution satellite imagery for improved geo-positioning accuracy. ISPRS J. Photogramm. Remote Sens. **114**, 125–136 (2016)
36. Y.H. Jiang, J.Y. Wang, L. Zhang, G. Zhang, X. Li, J.Q. Wu, Geometric processing and accuracy verification of Zhuhai-1 hyperspectral satellites. Remote Sens. **11**(9), 996–1013 (2019)
37. B. Yang, M. Wang, Y.D. Pi, Block-adjustment without GCPs for large-scale regions only based on the virtual control points. Acta Geod. Cartogr. Sin. **46**(7), 139–151 (2017)
38. B.W. Liu, X.J. Duan, L. Yan, A novel Bayesian method for calculating circular error probability with systematic-biased prior information. Math. Probl. Eng. **2018**, 1–10 (2018)
39. D.E. Chaitanya, L. Ganseh, G.S. Rao, Performance analysis of hyperbolic multilateration using circular error probability. Procedia Comput. Sci. **85**, 676–682 (2016)
40. C.H. Grohmann, Evaluation of TanDEM-X DEMs on selected Brazilian sites: comparison with SRTM, ASTER GDEM and ALOS AW3D30. Remote Sens. Environ. **212**, 121–133 (2018)
41. B. Wessel, M. Huber, C. Wohlfart, U. Marschalk, D. Kosmann, A. Roth, Accuracy assessment of the global TanDEM-X digital elevation model with GPS data. ISPRS J. Photogramm. Remote Sens. **139**, 171–182 (2018)
42. D.B. Gesch, D.F. Maune, *Digital Elevation Model Technologies and Applications: The DEM Users Manual The National Elevation Dataset*, 2nd edn. (American Society for Photogrammetry and Remote Sensing, Bethesda, 2007), pp. 99–118

Publisher's Note

Springer Nature remains neutral with regard to jurisdictional claims in published maps and institutional affiliations.